Cosmic ray composition from multiple muon data with the KGF underground detector

H. R. Adarkar, S. R. Dugad, M. R. Krishnaswamy, M. G. K. Menon, N. K. Mondal, V. S. Narasimham, and B. V. Sreekantan
Tata Institute of Fundamental Research, Homi Bhabha Road, Bombay, India 400 005

Y. Hayashi, N. Ito, S. Kawakami, S. Miyake, and Y. Uchihori
Osaka City University, Osaka 558, Japan

(Received 27 August 1997; published 6 February 1998)

The Kolar Gold Field (KGF) experiment was operated for about 6 years at a depth of about 6045 hg/cm^2 using a calorimetric, fine-grain detector and recorded 307 multiple muon events in addition to about 23000 single muons. The mean sea level energy of muons arriving vertically at this depth being around 7 TeV, one has a sensitive probe for the chemical composition of primary cosmic rays at energies around the *knee* in the energy spectrum. Predictions based on several rigidity dependent composition models are compared with observed multiplicity spectrum. The data strongly support a mixed chemical composition with medium to heavy primaries contributing substantially beyond 10^{15} eV. The proposed model explains all the features of the data and is consistent with the results from direct measurements as well as the all particle energy spectrum. [S0556-2821(98)00207-0]

PACS number(s): 96.40.De, 13.85.Tp, 96.40.Pq, 96.40.Tv

I. INTRODUCTION

The primary cosmic ray spectrum has been determined over the energy range 10^8–10^{20} eV, using a variety of techniques. The spectrum in the different energy ranges can be expressed in the form of a power law $E^{-\gamma}$ with different values of the exponent in different energy ranges. Two very pronounced changes occur, one around 10^{15} eV where the spectrum steepens and another around 10^{18} eV where the spectrum tends to flatten. The first is called the *knee* and the second the *ankle* of the primary spectrum.

It has been possible to determine the composition of the primary cosmic rays (PCRs) through direct measurements with balloon- and satellite-borne instruments only up to the energy range of $\sim 10^{14}$ eV. Beyond this, direct measurements are not feasible because of a steeply falling flux of the primary radiation. The presence of the *knee* in the spectrum is believed to be connected with a change of composition of the primary radiation. Evidence is gradually accumulating to suggest that the composition is changing even around $\sim 10^{14}$ eV, a decade earlier than the knee region.

The only method available for the determination of the composition around the knee region is the method of extensive air showers through a measurement of the different features of the various secondary components such as electrons, muons, hadrons, etc. Detailed Monte Carlo simulations have shown that one of the suitable components of the air shower from the point of view of the primary composition is the high energy muon component, especially the multiplicity spectrum of high energy muons. In this paper we discuss the results that have emerged from the study of multiple muon events recorded in the deep underground Kolar Gold Field (KGF) detector. The Phase-2 detector is larger among all those employed here and data from this detector are used for the present study.

II. DATA REDUCTION

The KGF underground detectors were situated in deep mines at 12°57N geographic latitude and 78°18E longitude with a flat surface terrain located 900*m* above m.s.l. The instrumentation and data acquisition system of the Phase-2 detector has been published in full detail in [1]. The main detector is made up of 60 horizontal layers of sealed proportional counters, separated by 6 mm thick iron slabs. Each layer consists of 58 proportional counters, filled with *P*10 gas (90% Ar + 10% CH_4) at a pressure of 85 cm of Hg. These layers are stacked in an orthogonal geometry in order to get a stereoscopic view of tracks. The main detector is surrounded by a *jacket* of vertical columns on three sides which serves as an offline veto for a proton decay search. Each side has two vertical columns of proportional counters consisting of about 60 counters with a 1-in. Fe absorber between these columns. A schematic view of the complete Phase-2 detector is shown in Fig. 1. Various trigger criteria were employed to detect penetrating muons, contained events, etc. Full detection efficiency[1] for tracks due to atmospheric muons was achieved by keeping sufficiently loose trigger criteria. Salient features of the site, detector, and data are summarized in Table I.

We have analyzed the entire data recorded during the period of December 1985 to October 1992, corresponding to a total live time of 5.54 years. About 23 500 events, mostly due to single muons, were recorded during this period. The accuracy in the zenith angle is estimated as 0.7° for tracks with a path length $\geqslant 2$ m inside the detector. The zenith angle distribution of the single muon rate, shown in Fig. 2, is

[1]A pretrigger transistor-transistor logic (TTL) output pulse of 3 μsec width is generated independently for each layer in the main detector by taking the OR output of all the 58 counters in a layer. Thus, the presence of a hit in any counter would generate the pretrigger output for the corresponding layer. A muon trigger is generated whenever five such pretrigger pulses out of any consecutive 11 layers form a coincidence within a window of 3 μsec. Such loose criteria for the trigger (any 5 out of 11 layers) ensures almost 100% efficiency for detection of muons.

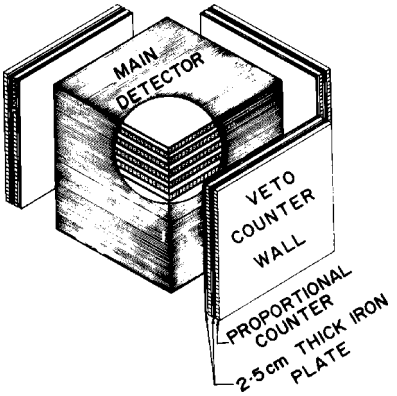

FIG. 1. Schematic view of the Phase-2 detector.

obtained by binning data in 5° intervals. The expected event rate due to atmospheric muons (shown as solid line) is obtained using an empirical form [2] for KGF rock and the detector aperture applicable for each angular bin. Large angle tracks beyond 60° are mostly due to a ν_μ ($\overline{\nu_\mu}$) interaction in the surrounding rock, producing muons which give rise to a penetrating track in the detector. The contribution from this phenomenon, shown as dashed line, is estimated using the ν_μ ($\overline{\nu_\mu}$) energy spectrum, its interaction cross section, etc. [3]. It can be seen that the total expected rate agrees well with the observations, confirming the satisfactory performance of the detector during the entire period.

A. Multiple muon analysis

We have observed 307 events called *multiple muons*, with well-separated tracks, parallel within the angular resolution of the detector, due to two or more muons passing through the detector. The contribution from pions produced in the rock by a photonuclear interaction of muons in the surrounding rock and mimicking multiple muon events is estimated to be quite small [4]. The observed multiple muon data extend smoothly up to the multiplicity $n_\mu=6$ except for one event with a very high multiplicity of 20^{+2}_{-1} [5]. Because of the good spatial resolution ($\sim$10 cm) of the detector, multiplicity could be easily determined for events with a track separation larger than 10 cm. Since the separation between muons for the Phase-2 depth is typically 150 cms, the number of multiple tracks with a separation $<$10 cm would be negligibly small. Table II shows the observed multiplicity distribution of muons. Because of the finite size of the detector, all the muons in a multiple muon event may not pass through the detector. Thus, the observed multiplicity distribution is not the same as a *true* multiplicity distribution. The geometrical efficiency of the detector, i.e., the containment probability $P_{geom}(n_\mu/n'_\mu)$ of observing an event of actual multiplicity n'_μ as n_μ is obtained using the decoherence curve and the lateral distribution of multiple muons for each multiplicity. The expected multiplicity distribution applicable to the Phase-2 detector geometry and depth is obtained by applying geometrical corrections to the true multiplicity distribution evaluated for a given composition model; this is then compared with the observations.

TABLE I. Experimental details of the Phase-2 detector at KGF.

Depth	6045 hg/cm^2
KGF rock density	3.03 g/cm^3
KGF rock $\langle Z/A\rangle$	0.495
KGF rock $\langle Z^2/A\rangle$	6.4
Basic detection unit	Proportional counter
	10 cm$\times$10 cm$\times$6 m
Detector dimensions	$6\times6\times6.5$ m^3
Number of counters	3834
Number of layers	60 + 6 (veto jacket)
Angular resolution	0.7°
	(Path length $>$ 200 cm)
Spatial resolution	10 cm
Total weight	320 tons
Live time	5.536 years
Total number of muons	23151 ($\theta<50°$)
Number of multiple muons	307

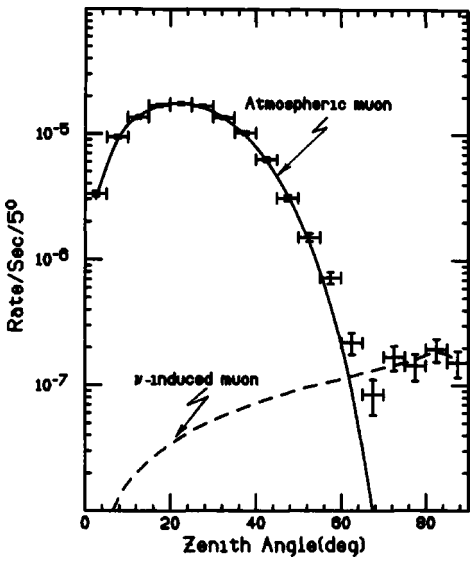

FIG. 2. Zenith angle distribution of single muons.

B. Geometrical correction for $n'_\mu=2$

The decoherence distribution for $n_\mu=2$ data, obtained by calculating the spatial separation $D_\perp$ between two muon tracks and grouping them in 50 cm bins, is used to estimate the geometrical correction for $n'_\mu=2$. The probability $p(D_\perp,\theta)$ of recording events with the true multiplicity, i.e.,

TABLE II. Observed multiplicity distribution.

Multiplicity n_μ	Observed number of events
1	22 844
2	265
3	33
4	6
5	1
6	1
20^{+2}_{-1}	1

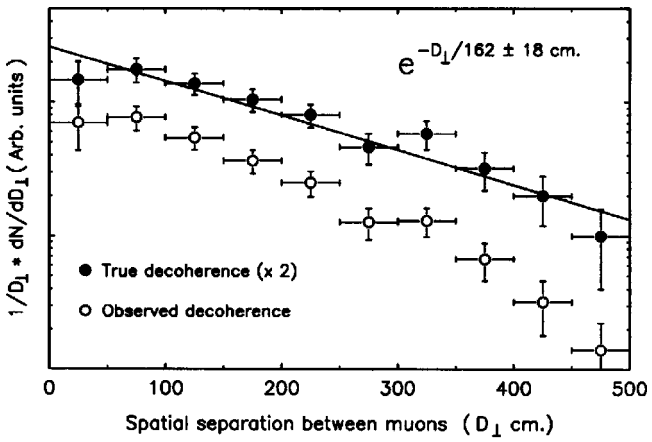

FIG. 3. The observed and the true decoherence distribution of muons. The solid line represents a fit of the exponential form.

$n'_\mu = n_\mu$ for $n_\mu = 2$, is obtained as a function of the spatial separation and zenith angle using the Monte Carlo method described in [4]. The containment probability is not sensitive to the azimuth ϕ due to the cubical geometry of the detector. However, it reduces rapidly with the separation and increases slowly with the zenith angle. The true decoherence distribution is obtained by appropriately normalizing the observed distribution with $p(D_\perp, \theta)$. The observed and true decoherence distributions are shown in Fig. 3. The solid line in the figure represents the exponential ($e^{-D_\perp/D^*_\perp}$) fit to the true decoherence with $D^*_\perp = 162 \pm 18$ cm. The ratio of the integral under the curves of the true and observed decoherence distributions gives the geometrical correction factor for $P_{geom}(2/2) = 0.583$ and hence $P_{geom}(1/2) = 0.417$. The systematic error due to averaging of $p(D_\perp, \theta)$ over a few angular ranges and extrapolation of the decoherence curve for integration is of the order of 5%.

C. Geometrical correction for $n'_\mu \geq 3$

Higher multiplicity data are corrected using the lateral distribution of muons, assumed to follow the same functional form as that derived from the p_t distribution of secondary particles produced in strong interactions. The value of r_0 varies as a function of depth. For Phase-2 depth, r_0 is obtained indirectly by simulating the true decoherence distribution for $n_\mu = 2$ data using the exponential form of the lateral distribution for different values of r_0 between 70 and 120 cm. We find that $r_0 = 90 \pm 10$ cm generates the observed value of $D^*_\perp$ to a good approximation. Thus, the lateral distribution function of muons, $f(r)$, consistent with the observed data, is given by

$$f(r) \propto \frac{1}{r} e^{-r/r_0}, \quad r_0 = 90 \pm 10 \text{ cm}. \tag{1}$$

The overall containment probability $P_{geom}(n_\mu/n'_\mu)$ at higher multiplicity ($n'_\mu \geq 3$) is obtained by using this lateral distribution through a Monte Carlo method. The procedure adopted to obtain $P_{geom}(n_\mu/3)$ is as follows.

(a) Project the detector in a plane perpendicular to the shower axis, say, at an angle θ.

TABLE III. Average containment probability $P_{geom}(n_\mu/n'_\mu)$ for the Phase-2 detector.

True multiplicity n'_μ	Observed multiplicity n_μ 1	2	3	4	5	6
2	0.417	0.583	-	-	-	-
3	0.299	0.251	0.450	-	-	-
4	0.283	0.154	0.205	0.358	-	-
5	0.275	0.115	0.115	0.185	0.310	-
6	0.269	0.106	0.077	0.100	0.171	0.277

(b) By randomly selecting a point on the plane, generate three other points with respect to it using the lateral distribution function [Eq. (1)] with the value of r_0 chosen between 80 and 100 cms. Only those samples in which at least one out of three points falls on the shadow area of the detector are accepted as *meaningful* samples. A large number of such samples are generated.

(c) The containment probability is obtained as a function of r_0 and θ for different observed multiplicities by taking the ratio

$$P(n_\mu/3, r_0, \theta) = \frac{N(n_\mu)}{\text{total number of samples}}, \tag{2}$$

where $N(n_\mu)$ is the number of samples with n_μ points ($1 \leq n_\mu \leq 3$) inside the shadow area of the detector. The probability is observed to vary gradually with these parameters. Geometrical corrections up to $n'_\mu = 6$ are obtained by adopting a similar procedure. They are averaged over θ and r_0 (Table III) and used to compute the expected multiplicity distribution applicable to the geometry of the Phase-2 detector for different composition models. The error on $P_{geom}(n_\mu/n'_\mu)$ due to averaging is between 6% and 10% for $n'_\mu = 3$–6.

III. SIMULATION OF THE MULTIPLICITY DISTRIBUTION

The multiplicity distribution for the Phase-2 detector is estimated through the simulation of the high energy muon component of extensive air shower (EAS) for all components of the composition model. It further involves the propagation of muons through rock to the depth of observation and parametrization of simulated data. The mean energy of muon reaching the depth of 2 km being around 7 TeV, one could confine the simulations to energies >3 TeV without any loss of accuracy. The entire scheme of simulation, parametrization, and estimation of the multiplicity distribution is implemented in the following steps.

(1) Simulation of hadronic showers in the atmosphere. The Monte Carlo code basically simulates the interactions of primary as well as secondary particles with air nuclei and follows all particles that could give rise to high energy muons ($E_\mu > 3$ TeV) up to the surface of the mine. The code has the following features.

(a) For a given primary nucleon, the interaction point in the atmosphere is generated using the energy-dependent cross section and the atmospheric model which gives the depth profiles in units of g/cm^2, expressed as a function of

altitude and zenith. The energy dependence of the interaction mean free path for various hadrons, as given in [7], has been used in the present calculation. For primary nuclei, a fragmentation model is used to break up the nuclei into nucleons and generate their interactions points in the atmosphere (see Appendix A).

(b) The HADINT routine (see Appendix A) is then called to simulate the interaction for a given input laboratory energy; this produces secondary particles of different types with their momenta and particle identification as its output. The interaction routine is based on the accelerator data on $p\bar{p}$ collisions described in Appendix A. The same routine also simulates the production of *charm* mesons which could give rise to muons through their relatively fast decays. These are referred to as *prompt* (or *direct*) *muons* and their contribution to the total observed flux is studied separately. All the *neutral* pions as well as particles with energy <3 TeV are ignored after their production to economize the computing time. It may be noted that the survival probability of muons with energy <3 TeV at Phase-2 depth is too small ($<10^{-5}$) and hence their contribution to the expected muon flux is insignificant.

(c) Charged pions or kaons can either interact or decay in the atmosphere; their decay as well as interaction lengths are generated using the Lorentz-boosted lifetime and the interaction cross section. They are made to interact or decay depending on whichever occurs first. For interacting particles, HADINT is called again and for decaying particles all the information such as point of production, momentum, etc., is stored for muons with energy more than 3 TeV. This procedure is followed until all the particles in EAS have energy <3 TeV.

(2) A large number of showers are simulated for all components of primaries (broadly grouped as p, He, CNO, Mg-Si, and Fe) at several discrete energies (10^{13}–10^{17} eV) and zenith angles. Since showers are simulated at discrete energies and zenith angles, simulated data on multiplicity distribution and energy spectrum of muons at the ground level are parametrized in order to generate muons and their energy at intermediate primary energies and zenith angles (see Sec. III A).

(3) Next the muon multiplicity and its energy for a large number of samples are generated for a given primary at finer energy intervals in each zenith angular bin of 5° up to 50° and propagated to the depth of observation using accurate calculations on the survival probability of muons (see Appendix B). It may be noted that the observed data are also grouped into similar angular bins.

(4) The probability functions $P_j(n'_\mu, E_n, \theta_i)$ are obtained for each primary from the multiplicity distribution of muons reaching the detector depth. These functions give the probability of recording an event of true multiplicity n'_μ, from a primary of type j and energy E_n, penetrating through slant depth corresponding to the Phase-2 detector depth for an angular bin θ_i (see Sec. III B).

(5) Finally, the probability functions and geometrical correction factors are used to numerically compute the expected multiplicity distribution for different composition models (see Secs. IV and V) and compared with the observations.

TABLE IV. Best fit coefficients to calculate the average multiplicity (E_n is in TeV/nucleon), $\log_{10}\langle N_\mu(>3\ \text{TeV})\rangle = \sum_{i=0}^{4} a_i [\log_{10} E_n]^i$.

Primary	a_0	a_1	a_2	a_3	a_4
p	-6.7536	5.9104	-2.3224	0.45286	-0.03211
α	-6.7241	6.571	-2.6243	0.51175	-0.03612
CNO	-7.7334	9.865	-4.9939	1.2139	-0.109
Mg-Si	-6.7251	8.2728	-3.8488	0.87347	-0.07357
Fe	-6.0274	7.3786	-3.1621	0.6608	-0.05073

A. Simulation and parametrization

The PCR composition is studied in terms of five dominant components of cosmic rays, viz., p, α, CNO, Mg-Si, and Fe. A large number of showers are simulated for these primaries at discrete energies ranging from 10^{13} to $\sim 10^{17}$ eV at zenith angles $\theta = 10°$, 20°, and 30°. The simulated data basically contain the information on the average multiplicity of muons $\langle N_\mu(>3\ \text{TeV})\rangle$, the multiplicity distribution, and the energy spectrum of muons at the surface of mines. The zenith angle dependence of the average multiplicity for a given primary energy is observed to be consistent with the well-known $\sec\theta$ law. The $\langle N_\mu(>3\ \text{TeV})\rangle$ in the vertical direction is expressed in terms of the primary energy as a fourth degree polynomial of the primary energy; the coefficients of the fit for various primaries are given in Table IV. Using these and the $\sec\theta$ law, the average multiplicity of muons could be obtained for a given primary energy and zenith angle. The dependence of average multiplicity on the primary energy is shown in Fig. 4(a). The multiplicity distribution of simulated muons (>3 TeV) at the ground level is observed to fit a *negative binomial distribution* (NBD) as given in Eq. (A2).

The *shape* parameter k, of the NBD at each primary energy, is obtained by fitting the multiplicity distribution of

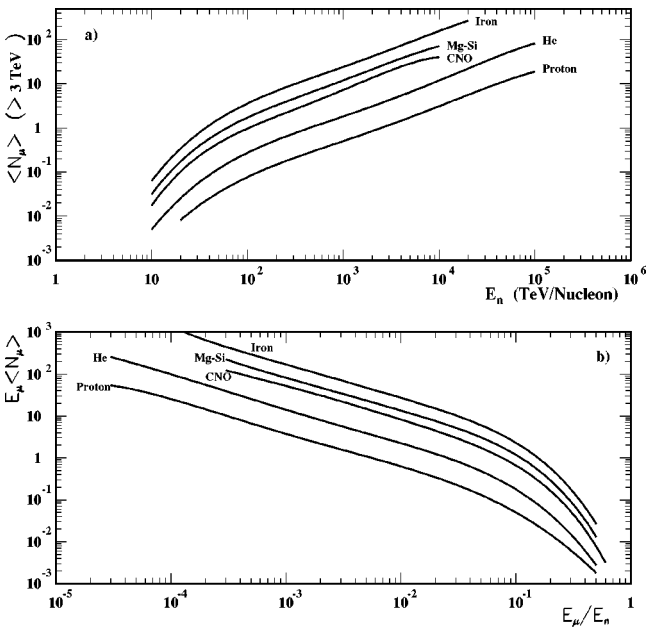

FIG. 4. Parametrization of simulated data. (a) Energy dependence of average multiplicity of muons and (b) energy spectrum of muons for various primaries.

TABLE V. Best fit coefficients to calculate the k parameter (E_n is in TeV/nucleon), $\log_{10}k=\Sigma_{i=0}^{2}b_i[\log_{10}\langle N_\mu(E_\mu>3$ TeV, $E_n,\theta)\rangle]^i$.

Primary	b_0	b_1	b_2
p	0.8094	0.3274	0.06823
α	1.1136	0.3503	0.07775
CNO	1.1624	0.6215	-0.00295
Mg-Si	1.0627	0.4687	-0.012
Fe	0.9515	0.3093	0.11027

simulated muons and is expressed in terms of the primary energy E_n (TeV/nucleon), using a second degree polynomial fit (Table V). By obtaining the average multiplicity and the k parameter using the coefficients in Tables IV and V, we can generate the number of muons with energy >3 TeV for any primary of a given energy E_n, arriving at an angle θ. In order to get the energy spectrum of muons, the data are parametrized in an indirect manner. Figure 4(b) shows the plot of $\langle N_\mu\rangle\times E_\mu$ versus E_μ/E_n, where $\langle N_\mu\rangle$ is the average multiplicity of muons at the sea level with an energy more than E_μ (TeV). At each primary energy, $\langle N_\mu\rangle$ is obtained from simulated data, at different energy thresholds ranging from 3 to 30 TeV. These are fit to a polynomial with the coefficients as given in Table VI. Muons in EAS could now be generated at any given primary energy and zenith angle by generating a number of muons (>3 TeV) as described above and then distributing energy to these muons using the energy spectra from the parametrization given in Table VI. We have also simulated showers by including the nuclear target effect (Appendix A) and the results are parametrized in a similar manner.

B. Estimation of probability functions $P_j(n'_\mu,E_n,\theta_i)$

The probability functions are obtained for ten angular bins of 5° width and up to the true muon multiplicity of 6. The number of muons and their energy are generated using the parametrization described in the previous section for fixed primary energy and angular bin. These muons are propagated through the slant depth corresponding to the angular bin using the detailed survival probability calculation (Appendix B). A large number of such samples are generated and then $P_j(n'_\mu,E_n,\theta_i)$ for a primary of type j is calculated at a given

TABLE VI. Best fit coefficients to calculate $E_\mu\langle N_\mu\rangle$ (E_μ is in TeV and E_n is in TeV/nucleon), $\log_{10}E_\mu\langle N_\mu\rangle=\Sigma_{i=0}^{5}c_i[\log_{10}E_\mu/E_n]^i$.

Primary	c_0	c_1	c_2	c_3	c_4	c_5
p	-3.6628	-3.3760	-1.2111	-0.1944	.005791	0.002911
α	-3.9346	-5.3749	-2.9961	-0.9393	-0.1408	-0.008104
CNO	-3.8034	-6.8973	-4.8817	-1.981	-0.4013	-0.03203
Mg-Si	-3.5678	-6.8586	-4.7365	-1.8578	-0.3665	-0.02905
Fe	-3.2181	-6.6695	-4.5269	-1.7508	-0.3391	-0.02624

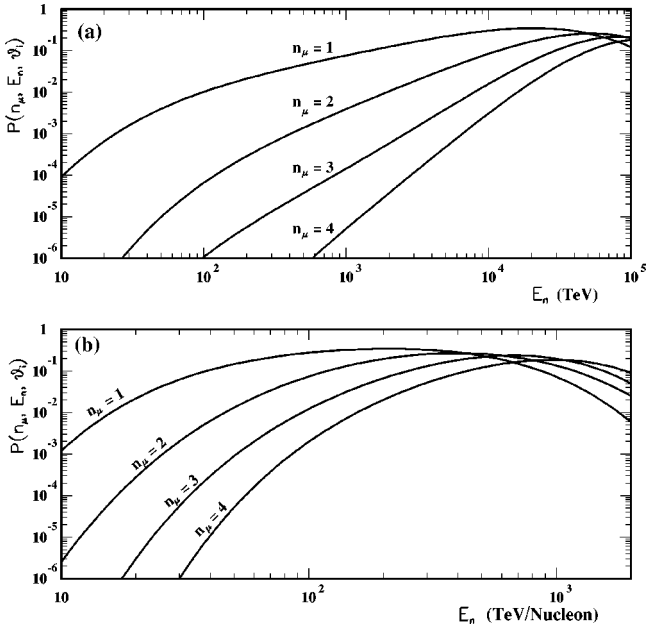

FIG. 5. Probability distribution at observational depth in the near vertical direction for different multiplicities of muons plotted against the primary energy for (a) proton and (b) iron primaries.

energy E_n by finding the fraction of the number of samples giving muons of true multiplicity n'_μ. In this manner, $P_j(n'_\mu,E_n,\theta_i)$ is determined for a muon multiplicity up to 6, at several energies for the same type of primary and slant depth, which is then parametrized as a function of primary energy for each multiplicity.

To ensure the validity of this parametrization, we have propagated the muons simulated at discrete primary energies at the sea level down to the depth of observation. The probabilities thus obtained are found to be in good agreement with the parametrization described above. As an example, Fig. 5 shows the probability of surviving muons up to a multiplicity of 4 in showers generated by proton and iron primaries as a function of the primary energy for the near vertical direction.

IV. SENSITIVITY OF DATA FOR COMPOSITION STUDY

Before studying different composition models, we examine the sensitivity of the observed data for different primaries. For this purpose, we obtained the expected multiplicity distribution for a pure composition, i.e., assuming that cosmic rays consist of only one type of primaries such as p or α, etc. The shapes of expected and observed multiplicity distributions are compared to see the sensitivity of data on the nature of the primary. We have assumed a power law form for the energy spectrum of the primary and then the expected multiplicity distribution is evaluated for different values of spectral indices. Let $\phi_j=K_jE^{-\gamma}$ be the differential energy spectrum of primaries of type j. The coefficient K_j is determined by normalizing the expected flux of single muons to the observed flux. This compensates for the uncertainties in the interaction model to some extent. The expected flux of

muons up to an observed multiplicity of 6 is calculated numerically in each angular bin as follows:

$$f_j(n_\mu,\theta_i)=K_j\sum_{n'_\mu=1}^{6}P_{geom}(n_\mu/n'_\mu)\times\int_{3\,\mathrm{TeV}}^{\infty}P_j(n'_\mu,E_n,\theta_i)E_{tot}^{-\gamma}dE_{tot},\qquad(3)$$

where $E_n=E_{tot}/A$. Contributions from a higher multiplicity ($\geqslant 7$) are much smaller than the statistical errors in the observations and hence they are neglected. The total expected number of single muon events ($n_\mu=1$) can then be obtained by summing over all angular bins as

$$n^j_{expt}(1)=T\sum_{i=1}^{10}f_j(1,\theta_i)A(\theta_i),\qquad(4)$$

where $A(\theta_i)$ is the integrated aperture area for angular bin θ_i and T is the total live time of the detector. K_j is found by normalizing $n^j_{expt}(1)$ with $N_{obs}(1)$.

Once K_j is known, the expected number of events of higher multiplicity can be obtained as

$$n^j_{exp}(n_\mu)=T\sum_{i=1}^{10}A(\theta_i)f_j(n_\mu,\theta_i)\qquad(5)$$

The ratio

$$R_j(n_\mu)=\frac{N_{obs}(n_\mu)}{n^j_{expt}(n_\mu)}\qquad(6)$$

up to multiplicity $n_\mu=4$ is obtained for each primary at different values of γ. Since only one event each is observed at a multiplicity of 5 and 6, the data at these multiplicities are not used for a comparison between the observed and expected multiplicity distributions. It is to be noted that $R(1)$ will be always 1 due to the normalization at $n_\mu=1$. If the data were not sensitive to the nature of primaries of different atomic weights, we would have expected the same shape of the $R(n_\mu)$ distribution for all primaries. Our results, shown in Fig. 6, indicate that the normalized expected multiplicity distribution is steeper as compared to the observation, for a lighter primary like a proton, whereas it is flatter for the Fe primary. A similar trend is seen for other primaries like α, CNO, and Mg-Si, confirming the sensitivity of the data to the composition. We have done this analysis by using the interaction model with and without the nuclear target effect, but the sensitivity to the composition is unaffected.

V. COMPOSITION MODELS AND COMPARISON WITH OBSERVATIONS

We have considered here three different composition models (Table VII) discussed in the literature [8]. They include the proton-dominated model suggested by Fichtel and Linsley as well as the heavy primary-dominated composition (Maryland model). In these models, the knee in the energy spectrum is assumed to be rigidity dependent. The predictions on the zenith angle distribution, lateral distribution, and

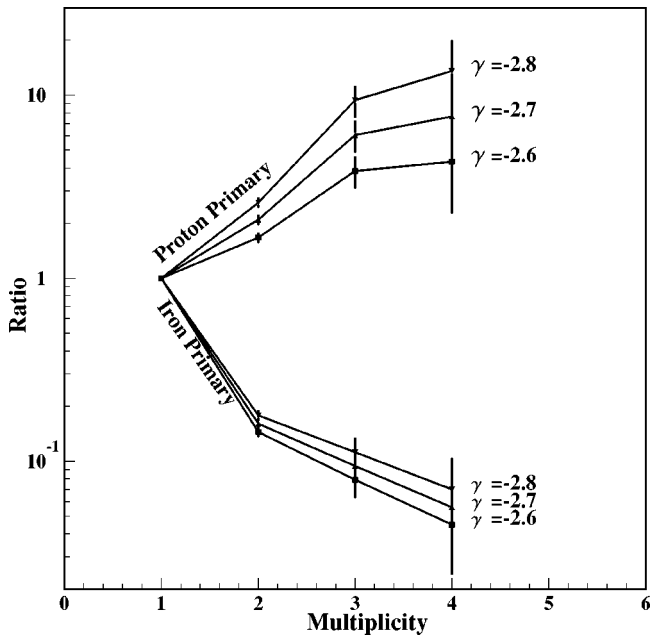

FIG. 6. The ratio of the observed to the normalized expected flux of muons at different multiplicities for a light and heavy primary.

multiplicity distribution of muons are compared with the data. The general method to obtain the expected multiplicity distribution for a given composition model is quite similar to the procedure described in Sec. IV. The resultant multiplicity distribution $[N_{expt}(n_\mu)]$ is obtained by evaluating $n^j_{expt}(n_\mu)$ using Eqs. (3) and (5) for each primary of type j and then summing it over all the primaries. The model dependence of the interactions and the uncertainty in the flux of cosmic rays have been reduced to a large extent by normalizing the expected single muon flux with that of observations. The nor-

TABLE VII. Primary composition models.

Composition	Group	K[a] (10^2)	γ $E<E_c$	E_c (10^5 GeV)	γ $E>E_c$
	p	172	2.71	20	3.00
	α	92.0	2.71	40	3.00
Constant mass	CNO	62.0	2.71	140	3.00
	Mg	92.0	2.71	260	3.00
	Fe	62.0	2.71	520	3.00
	p	260	2.73	1.0	
		18.4	2.50	100	3.02
	α	81.6	2.73	10	3.23
Linsley	CNO	56.5	2.73	35	3.23
	Mg	73.0	2.73	70	3.23
	Fe	63.3	2.73	130	3.23
	p	198	2.75	3.0	3.35
	α	103	2.77	6.0	3.37
Maryland	CNO	21.5	2.60	21	3.20
	Mg	11.4	2.50	42	3.10
	Fe	5.95	2.50	84	3.10

[a]K is in units of $\mathrm{m}^{-2}\ \mathrm{s}^{-1}\ \mathrm{sr}^{-1}\ (\mathrm{GeV/nucleus})^{-1}$.

TABLE VIII. Multiplicity distribution for various composition models.

Composition model	Primary	Multiplicity n_μ 1	2	3	4	5	6
	p	13964	74.2	2.33	0.22	0.02	0.00
	α	1998	29.5	1.71	0.25	0.09	0.03
CMC	CNO	525	18.0	2.52	0.54	0.20	0.07
	Mg-Si	441	20.0	3.11	0.74	0.34	0.10
	Fe	138	10.3	2.11	0.53	0.29	0.10
	Total	17066	152	11.8	2.28	0.94	0.30
	normalized	22844	204	15.8	3.1	1.25	0.40
	p	31395	194	8.54	1.00	0.09	0.00
	α	1286	14.5	0.59	0.06	0.02	0.01
Linsley	CNO	345	9.4	0.97	0.17	0.05	0.01
	Mg-Si	253	9.9	1.23	0.24	0.10	0.03
	Fe	101	6.7	1.15	0.26	0.11	0.04
	Total	33381	234	12.5	1.7	0.37	0.09
	Normalized	22844	160	8.6	1.18	0.24	0.06
	p	9636	33.5	0.54	0.02	0.00	0.00
	α	923	8.9	0.39	0.22	0.01	0.00
Maryland	CNO	749	21.5	2.09	0.36	0.15	0.03
	Mg-Si	1027	46.2	5.97	1.20	0.47	0.14
	Fe	298	22.1	3.99	0.92	0.44	0.14
	Total	12633	132	13.0	2.72	1.07	0.31
	Normalized	22844	239	23.5	4.9	1.93	0.61
	Observed	22844	265	33	6	1	1

malized multiplicity distribution, used for comparison with the observations, is given by

$$N_{expt}^{norm}(n_\mu)=\frac{N_{obs}(1)}{N_{expt}(1)}\times N_{expt}(n_\mu). \tag{7}$$

Multiplicity distributions are computed for the three composition models separately with and without the *nuclear effect*. The resultant shape of the expected multiplicity distribution for any of these models was found to be more or less independent of the *nuclear target effect*. Table VIII shows the contributions to single and multiple muon fluxes due to each primary as well as the normalized multiplicity distribution for all the composition models under study. Systematic errors in the expected multiplicity distribution due to the uncertainties in geometrical correction factors are 5%, 6%, 8%, and 10% for a multiplicity of 3, 4, 5, and 6, respectively. These errors are propagated in calculating the errors in the ratio $R(n_\mu)$. Figure 7 shows plots of $R(n_\mu)$ for these models up to a multiplicity of $n_\mu=4$. The observations at higher multiplicity are not included due to large statistical errors in these points. However, the expected multiplicity distribution is obtained up to a multiplicity of 6 as shown in Table VIII.

A. Constant mass composition model

The salient features of the expected multiplicity distribution for the constant mass composition (CMC) model (Table VIII) are the following.

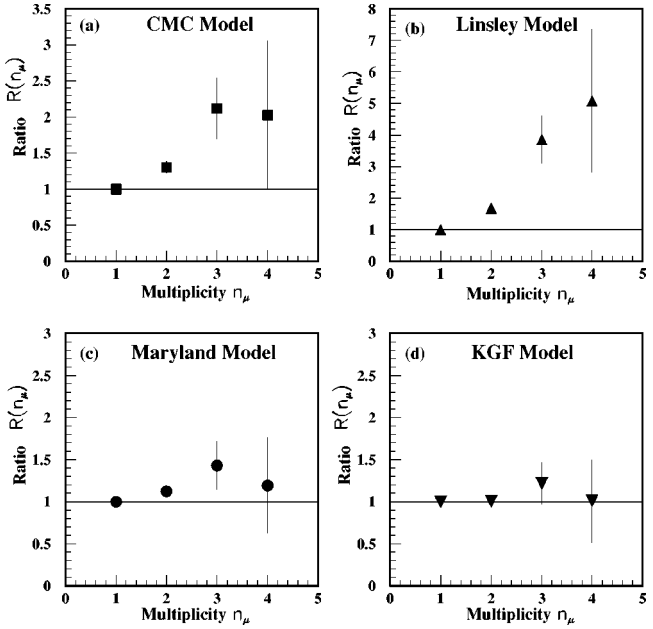

FIG. 7. Comparison of various composition models with observation.

The absolute flux of single muons is about 25% less than the observed flux but this can be accommodated within the uncertainties of K and γ in the composition model.

The contribution to the single muon flux is dominated by proton primaries, whereas helium and other heavy primaries dominate the higher multiplicity data.

The (normalized) expected multiplicity distribution is steeper as compared to observations. In Fig. 7(a), the ratio $R(n_\mu)$ is plotted as a function of n_μ up to multiplicity $n_\mu=4$. If the model was consistent with observations, the ratio should have been unity within the errors for each multiplicity but it can be seen that the observed multiplicity distribution clearly deviates from the expected values shown as a solid line in the figure. Thus the CMC model does not reproduce the observed multiplicity distribution.

The true composition model must therefore be richer in heavy elements than the CMC model to be able to reproduce the rate of high multiplicity events recorded in this experiment.

B. Linsley's composition model

Comparison of the observed and the expected multiplicity distributions obtained for this model (Table VIII) leads to the following conclusions.

The total number of expected single muons is much higher than the observed number. This is because the composition is very rich in primary protons, which are quite efficient in producing single muons.

The expected normalized multiplicity distribution is much steeper than the observations. The ratio $R(n_\mu)$ plotted up to $n_\mu=4$ in Fig. 7(b) shows a significant deviation from unity, represented by a solid line. Hence, this model does not explain the observed data satisfactorily.

Comparison of the multiplicity distributions obtained with the CMC and Linsley's models indicates that the latter has larger deviations from the observation. This is because Linsley's model is richer in protons than the CMC model. The

data strongly suggest that the actual composition must be more abundant in heavy elements than that predicted in these two models.

C. Maryland composition model

This model is based on the experiments in which delayed hadrons were studied in air showers [9] and suggests a heavy composition beyond the knee region. The multiplicity distribution computed for this model is given in Table VIII and compared with the observed distribution below.

The expected number of events at each multiplicity are quite small ($\sim 50\%$) as compared to the observations. It may be difficult to attribute this discrepancy completely to the uncertainties in the interaction model and the primary spectrum itself. However, the fluxes of various primary components for this model, below the knee (which contributes mostly to the single muon flux), are more or less consistent with the observations from direct measurements which extend up to ~ 100 TeV.

The normalized (expected) multiplicity distribution is, however, close to the observation as seen from the ratio $R(n_\mu)$ plotted in Fig. 7(c). Hence, the Maryland model reproduces the shape of the observed multiplicity distribution.

It is thus clear that, the Maryland composition model will be viable at these high energies if one can enhance the absolute fluxes so as to be in agreement with the present observation. This can be partly accomplished by shifting the knee in the energy spectrum to a higher value so that the flux of protons and subsequently other elements beyond $300Z$ TeV would increase, thereby enhancing the expected flux of muons.

There are some other features of the predictions of the models discussed above which are found to be consistent with the observations for all the models and hence not sensitive enough to distinguish between these models. The shape of the zenith angle distribution of single muons predicted by all the models is consistent with the observations. Similarly, the lateral distribution obtained for various models using simulated data agrees well with that of observations. Inclusion of the *nuclear effect* gives a marginal change in the absolute flux but does not change the shape of the multiplicity distribution for any of these models. The contribution of *prompt muons* to the total flux is found to be quite small and it varies between 1.5% and 2%.

D. KGF composition model

This model is constructed to explain all features of the observations. It is based upon the recent data available from direct measurements in the multi-TeV primary energy region [10] and indirect measurements in the knee region. First, the differential spectral index as well as the flux of primaries is chosen to be consistent with the observations at lower energies. To begin with, the value of the rigidity dependent knee is assumed to be $E_c^p = 2000$ TeV. The proposed composition model is shown in Table IX. Expected multiplicity distribution obtained for this model is shown in Table X. It can be seen that the absolute flux of single muons is about $\sim 25\%$ lower than the observation which could be attributed to the uncertainties in the primary flux and the interaction model. The normalized multiplicity distribution is in good agreement with the observations. The data used to study the composition have been limited to a multiplicity of 6, of which the single muon data are used for normalization and only one event each is observed at a multiplicity 5 and 6. Because of this, we have used the same value of γ beyond the knee for all the elements, which is consistent with the spectral index of the all-particle energy spectrum.

The ratio $R(n_\mu)$ is consistent with unity within statistical errors as shown in Fig. 7(d). The zenith angle distribution of single muons and the lateral distribution are seen to be consistent with the observation. Hence, the composition model presented in Table IX explains all the features of the data adequately.

The sensitivity of the observed data to the *knee* position has been studied by obtaining the multiplicity distribution for different values of E_c^p in the energy spectrum of protons and correspondingly other primaries (using the rigidity dependence). The resultant multiplicity distribution for different values of E_c^p are shown in Table XI. It can be seen that for $E_c^p > 1000$ TeV the multiplicity distribution does not change much, but for $E_c^p < 500$ TeV the expected number of events

TABLE IX. KGF composition model.

Group	K[a] (10^2)	γ $E<E_c$	E_c 10^6 GeV	γ $E>E_c$
p	276	2.77	2.0	3.1
α	155	2.71	4.0	3.1
CNO	21.5	2.60	14	3.1
Mg	13.8	2.60	26	3.1
Fe	5.66	2.50	52	3.1

[a] K is in units of $m^{-2}\ s^{-1}\ sr^{-1}\ (GeV/nucleus)^{-1}$.

TABLE X. Multiplicity distribution for the KGF model.

Primary	Multiplicity n_μ					
	1	2	3	4	5	6
p	11508	54.6	1.65	0.15	0.15	0.00
α	4536	67.2	4.09	0.52	0.16	0.04
CNO	856	33.9	5.06	1.16	0.40	0.14
Mg-Si	361	19.0	3.13	0.77	0.32	0.11
Fe	348	31.6	6.98	1.97	1.11	0.38
Total	17609	206.3	20.9	4.57	2.01	0.67
Normalized	22844	268	27.1	5.93	2.61	0.87
Observed	22844	265	33	6	1	1

TABLE XI. Multiplicity distribution for the KGF model at different knee energies.

E_c^p (TeV)	Multiplicity n_μ			
	1	2	3	4
500	22398	231	20	4
1000	22732	254	24	5
2000	22844	268	27	6
Observed	22844	265	33	6

with $n_\mu=2$ differs more than 2σ from the observations. Though our data are sensitive only up to a primary energy of $\sim 10^{16}$ eV, a comparison between the KGF model in the very high energy region ($\sim 10^{17}$ eV) and the currently available all-particle energy spectrum suggests that E_c^p should be around 1000 TeV.

VI. DISCUSSION

The Phase-2 detector was operated successfully over a long period of time (1985–1992) at one of the largest depths (6045 hg/cm^2) in the world at the Kolar Gold Field mines in India. It has recorded about $\sim$23 000 single muons and 307 multiple muon events. The Monte Carlo simulation studies of multiple muons show that even the low multiplicity data obtained at these depths have a good sensitivity in probing the primary cosmic ray composition in the *knee* region. This is mainly because of the large depth of operation, detecting a multi-TeV muon component of the EAS generated in the first few interactions of the primary. The multiplicity distribution obtained by assuming a pure composition with any one of the five components of primary cosmic rays does not agree with the observation (Fig. 6).

Even if the composition, i.e., the energy spectra of various elements, is exactly known, the absolute flux of muons may not agree with that of observations. This could be due to uncertainties in the interaction model used in hadronic shower simulations. The interaction model is based upon $p\bar{p}$ collider data available up to $\sim$400 TeV in the laboratory frame and *p-air*, *nucleus-nucleus* collisions of much lower energies, beyond which reasonable extrapolations are made. In the present analysis, the uncertainties in the interaction model as well as in the flux of the cosmic rays in the assumed composition model are substantially compensated by normalizing the flux of single muons with that of observation. Therefore, it is actually the shape of the observed multiplicity distribution that is used for probing the cosmic ray composition rather than the absolute flux of the muons.

The proton-rich (Linsley model) and the constant mass composition models yield a steeper multiplicity distribution as compared to the observation and hence are not supported by our data (Fig. 7). For the Maryland model, the predictions agree with the data within 1.6σ. However, the expected fluxes are quite small compared to the observation. This could probably be attributed to the low rigidity cutoff used in this model. It has to be noted, however, that the fluxes of various elements in the Maryland model are consistent with the direct observations up to $\sim$100 TeV. Hence, a comparison of the multiplicity distribution for the Maryland model with the observations gives an indication of a *mixed* or *heavy* composition in the PeV energy region.

The proposed KGF model is based upon an extrapolation of the energy spectra observed so far by direct experiments ($\sim$100 TeV for lighter and $\sim$1 TeV/nucleon for heavier elements) to a higher energy region. Hence the spectral indices and the coefficients of power law energy spectra are known before the bend in the spectrum. Beyond the (rigidity-dependent) knee, we assumed the spectral indices of each of the five groups of elements to be same as that of the all-particle energy spectrum. The predicted flux of muons at all multiplicities up to $n_\mu=4$ is about 25% less. This could be well within the uncertainties in the primary flux and interaction model. The KGF model explains all features of the observations. The sensitivity of the data to the *bend* in the spectrum was studied by obtaining a multiplicity distribution at different values of the *knee* (Table XI). It is observed that the multiplicity distribution obtained with the knee around $1000Z$ TeV is consistent with observation as well as the all-particle energy spectrum at least up to 10^{17} eV. It can be seen from Table X that the flux of single muons is mostly dominated by protons and He, whereas all elements contribute significantly to $n_\mu=2$ data. Heavier elements start dominating with increasing multiplicity. Because of a limited number of constraints from the data, it will be more appropriate to get the global features of the KGF model by clubbing medium and heavy components (CNO, Mg-Si, and Fe) together. The relative abundance of the three groups estimated from the proposed KGF model is shown in Table XII at different primary energies. It can be clearly seen that this model gives rise to a *mixed* composition in the *knee* region which further becomes rich in heavy elements at higher energies. Furthermore, we have observed six events with multiplicity $\geqslant 5$ (out of which two events are contained in the main detector with no isolated tracks in the veto walls) when tracks passing through the veto walls without intercepting the main detector are also included in the multiplicity counting. This means that the number of events with true multiplicity $\geqslant 5$ is at least 6. Apart from this, we have observed one event with an anomalously high multiplicity ($n_\mu = 20^{+2}_{-1}$). Analysis of this event shows that, if this event is due to the *normal* hadron interaction, then it is more likely to be due to a heavy primary of energy $\sim 10^{17}$ eV [5]. Even though we cannot draw any firm conclusions based on high multiplicity data with low statistics, it does provide additional support to the proposed composition model.

TABLE XII. Composition at various energies in the KGF model.

Energy (TeV/nucleus)	Proton (%)	Helium (%)	Medium heavy + heavy (%)
100	29	32	39
1000	22	29	49
6000	12	20	68
10000	10	17	73

As mentioned before, the observations are interpreted through the simulation of hadronic showers. The interaction model is based on a simple extrapolation of available experimental data from accelerators, assuming no drastic change in the interaction characteristics at higher energies. We have studied the effect of the nuclear target but it does not change the shape of the expected multiplicity distribution significantly. The contribution from prompt muons is seen to be at the level of only a few percent.

Several underground experiments have reported their results recently. MACRO is the largest ($76.6\times 12\times 4.8$ m^3) among all other underground detectors; it is situated at an average depth of 3800 hg/cm^2 in a cavity under the mountainous terrain. Analysis of their data recorded with a full size detector using a multiparametric fit to multiple muons indicates a possible increase of the average mass number at

higher energies [11]. A combined analysis of data from the air shower array, EAS-TOP, with multimuon events in the MACRO detector disfavors pure proton or pure iron composition models. Instead, they favor a mixed composition in and around the knee [12]. Baksan experimental results are consistent with the extrapolation of the directly measured energy spectra in the energy range of 40–100 TeV/nucleon [13]. Results from the NUSEX group do not support a proton-dominant composition in the knee region [14].

ACKNOWLEDGMENTS

We wish to thank B. Satyanarayna, S. D. Kalmani, P. Nagraj, and L. V. Reddy for their able assistance in the maintenance of the detector and data collection, B. S. Acharya for his suggestions during the development of the Monte Carlo code and data analysis, S. C. Tonwar for providing a computing facility, and M. V. S. Rao, K. Sivaprasad, and B. K. Chatterjee for many useful discussions. We are thankful to the Ministry of Education, Japan for partial financial support. The cooperation of the officers and other staff of Bharat Gold Mines Ltd. at all stages of our experimental activity is gratefully acknowledged.

APPENDIX A

1. Simulation of nucleon-nucleon interaction (HADINT routine)

The hadron interaction routine is mainly based upon the data available from $p\bar{p}$ collider experiments up to laboratory energy of $\sim$400 TeV; these results are extrapolated to higher energies. It basically involves three steps: multiplicity generation for different particles like $\pi^{\pm}$, π^0, $K^{\pm}$, etc.; and transverse momentum (p_t) and pseudorapidity (η) generation for all (including leading) particles. Longitudinal momenta for all particles are calculated using their p_t and η. Transverse as well as longitudinal momenta are conserved while simulating the interaction.

a. Multiplicity generation

In our simulation we have considered only six types of secondaries, viz., $\pi^{\pm}$, π^0, $K^{\pm}$, $K,\bar{K}^0$, $p\bar{p}$, and $n\bar{n}$. Production of heavier baryons is ignored since their multiplicity is quite small. However, we have considered their contribution (through decay) to pions, kaons, etc. The production of charm particles is considered separately in view of their significant leptonic branching ratio and very short lifetimes. The inclusive average multiplicity $\langle n_{ch}\rangle$ of charged particles as a function of $\sqrt{s}$ fits reasonably well to a power law [15],

$$\langle n_{ch}\rangle = -7.0 + 7.2s^{0.127}. \tag{A1}$$

The ratio R_i, of individual multiplicity to the total charged multiplicity varies gradually with $\sqrt{s}$ and is fitted to a second degree polynomial in $\ln\sqrt{s}$. The average multiplicity for each type of secondary is obtained using $\langle n_{ch}\rangle$ and R_i. The number of baryons, kaons, or charm particles is obtained by fluctuating their respective $\langle n_i\rangle$ using a Poisson distribution. They are always produced in pairs. The charged multiplicity distribution containing mostly charged pions is seen to fit well with a *negative binomial distribution*, i.e.,

$$P(n,\langle n_{ch}\rangle,k) = {}^{n+k-1}C_{k-1}\left(\frac{\langle n_{ch}\rangle/k}{1+\langle n_{ch}\rangle/k}\right)^n\left(\frac{1}{1+\langle n_{ch}\rangle/k}\right)^k. \tag{A2}$$

The k parameter in Eq. (A2) defines the shape of the distribution which is fitted to [15]

$$k^{-1} = -0.014 + 0.058\ln\sqrt{s}. \tag{A3}$$

The numbers of charged as well as neutral pions are generated using the NBD.

b. Transverse momentum generation

Observed data from $p\bar{p}$ collider experiments show that $\langle p_t\rangle$ increases gradually with $\sqrt{s}$. The p_t distribution of secondary particles obeys an exponential form up to $p_t = 0.4$ GeV/c and a power law form for $p_t > 0.4$ GeV/c [16], i.e.,

$$\frac{d\sigma}{dp_t^2} = ae^{-bm_t} \quad (p_t \leqslant 0.4\ \text{GeV}/c)$$
$$= \left(\frac{p_0}{p_0+p_t}\right)^N \quad (p_t > 0.4\ \text{GeV}/c), \tag{A4}$$

where m_t ($=\sqrt{p_t^2+m^2}$) is the transverse mass of the particle, and p_0 is fixed at 1.3 GeV/c. The parameters a and b could be expressed in terms of N by using the continuity of $d\sigma/dp_t^2$ and its derivative at $p_t = 0.4$ GeV/c. Hence, N is the only free parameter which could be obtained by fitting the observed p_t distribution [16].

We have assumed here that $\langle p_t\rangle_{\pi^{\pm}} = \langle p_t\rangle_{\pi^0}$ and $\langle p_t\rangle_{p\bar{p}} = \langle p_t\rangle_{n\bar{n}}$. The free parameter N is fitted to a second degree polynomial in $\ln\sqrt{s}$ to get the p_t distribution at intermediate and higher energies.

After generating the number of secondary particles of different types, p_t for secondary as well as colliding particles are generated using the distribution given in Eq. (A4). The azimuthal angle ϕ_i is randomly generated between 0 to 2π for all but two particles. The azimuthal angles for the remaining two particles are calculated using the conservation of transverse momentum.

c. Pseudorapidity (η) generation

The observed *inclusive* η distributions at different c.m. system (c.m.s.) energies are available between ~ -5 and 5 up to $\sqrt{s} = 900$ GeV. They are fitted empirically to a *double Gaussian distribution* function as

$$\frac{1}{\sigma_{inel}}\frac{d\sigma_{inel}}{d\eta} = A\times\left[\exp\left(\frac{\eta-\mu}{\sigma}\right)^2 + \exp\left(\frac{\eta+\mu}{\sigma}\right)^2\right]. \tag{A5}$$

The free parameters are determined by fitting the observed η distribution at different accelerator energies [17]. These parameters are then fitted to a second degree polynomial in $\ln\sqrt{s}$. The parametrization of μ and σ is used to get the inclusive η distribution at intermediate or higher energies.

Pseudorapidity and hence longitudinal momenta for all the secondary particles are generated using the η distribution expressed in Eq. (A5). The longitudinal momenta for collid-

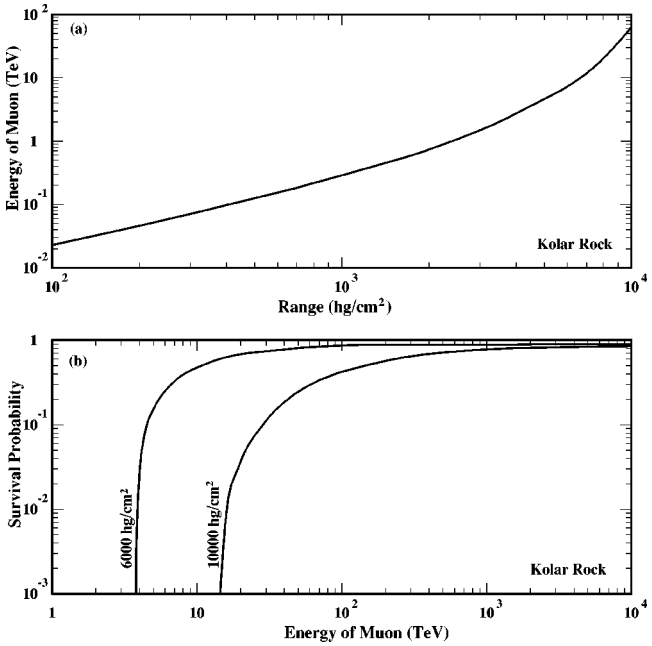

FIG. 8. Energy dependence of (a) range of muons and (b) survival probability of muons for a slant depth corresponding to a zenith angle of $\theta \sim 0°$ and $\sim 55°$ at Phase-2 detector depth.

ing particles are calculated using the conservation of longitudinal momentum and the total energy.

We have generated a large number of interactions at $\sqrt{s}$ = 200, 540, and 900 GeV. The multiplicity p_t and the inclusive η distributions obtained from simulations are seen to be consistent with the accelerator data. Also, the average inelasticity of collisions is found to vary between 0.45 and 0.51 in this energy region.

2. Colliding particle effect on interaction characteristics

From fixed target experiments on π^+-p and K^--p collisions, it has been observed that the interaction characteristics are similar to $p\bar{p}$ interactions at the same energy except for a reduction in the cross section [18]. In the HADINT routine we have treated the interaction characteristics of pions and kaons with nucleons in the same way as $p\bar{p}$ interactions.

As mentioned earlier the HADINT routine treats *proton-air* or *meson-air* collisions as *nucleon-nucleon* collisions except for the corresponding interaction cross sections. Accelerator data on heavy ion collision shows that the p_t distribution does not change significantly from $p\bar{p}$ data at a given energy [19] whereas the average multiplicity in the forward pseudorapidity region increases by $\sim 10\%$ with a moderate energy dependence [20] as

$$R_A = \frac{\langle n \rangle_{p\text{-}air}}{\langle n \rangle_{p\bar{p}}} = \frac{1}{2}(\bar{\nu} + 1), \tag{A6}$$

where

$$\bar{\nu} = 1.28 + 0.0214 \ln\sqrt{s}.$$

To study the effect of the nuclear target on the simulated high energy muon data, we have generated showers at a few energies, by incorporating the nuclear target effect as described above. We find that the nuclear target effect does not have much impact on the final conclusion regarding the primary cosmic ray composition. In simulating nucleus-air interactions, we have used the *fragmentation model* in which primary nuclei are split into nuclear fragments producing wounded nucleons, free nucleons, α particles, and heavy fragments [21]. The fragmentation probabilities are taken from nuclear emulsion chamber exposures in balloon flights [22]. Wounded nucleons, which travel in the backward hemisphere, have very small energies and hence are ignored. The heavy fragments interact further, producing smaller fragments ultimately splitting into nucleons. Hence, a primary nucleus of atomic weight A and energy E breaks into a system of A nucleons of energy E/A but at different depths in the atmosphere. Thereafter, we treat the *nucleon-air* interactions of A nucleons as discussed above.

APPENDIX B: ENERGY LOSS AND SURVIVAL PROBABILITY OF MUONS

Very high energy muons traversing matter lose energy primarily through bremsstrahlung, pair production processes and to a lesser extent through photonuclear processes; all these are subject to fluctuations. For the Phase-2 detector at KGF, the slant depth increases with zenith angle θ, almost as a linear function of $\sec\theta$, due to the fact that the surface terrain is almost flat to about 20 m up to $\theta = 50°$. The average energy of muons as a function of depth is shown in Fig. 8(a) and is between 8 and 40 TeV for the zenith angle range of $0°$–$50°$. The survival probability of these muons due to fluctuations in energy loss in a given thickness of rock has been evaluated earlier by Monte Carlo methods for KGF rock [6], where $\langle Z^2/A \rangle$ is 6.4, somewhat higher than that for so-called standard rock. The survival probability of muons is plotted in Fig. 8(b) as a function of muon energies for two slant depths corresponding to a zenith angle of $\theta \sim 0°$ and $\sim 55°$.

[1] H. R. Adarkar *et al.*, Nucl. Instrum. Methods Phys. Res. A **284**, 422 (1989); H. R. Adarkar *et al.*, Indian J. Pure Appl. Phys. **27**, 679 (1989); H. R. Adarkar *et al.*, Nucl. Instrum. Methods Phys. Res. A **308**, 574 (1991).
[2] S. Miyake, J. Phys. Soc. Jpn. **18**, 1093 (1963).
[3] H. R. Adarkar *et al.*, in *Cosmic Ray Conference, Proceedings of the 23rd International Cosmic Ray Conference*, Calgary, Canada, 1993, edited by R. B. Hicks *et al.* (World Scientific, Singapore, 1994), Vol. 4, p. 487.
[4] S. R. Dugad, Ph.D. thesis, University of Bombay, 1992.
[5] H. R. Adarkar *et al.*, Phys. Lett. B **267**, 138 (1991).
[6] M. R. Krishnaswamy, Ph.D. thesis, University of Bombay, 1981.
[7] G. B. Yodh, Yash Pal, and J. S. Trefil, Phys. Rev. D **8**, 3232 (1973); D. B. Keida, Ph.D. thesis, University of Pennsylvania, 1989.

[8] C. Forti *et al.*, Phys. Rev. D **42**, 3668 (1990); C. E. Fichtel and J. Linsley, Astrophys. J. **300**, 474 (1986); J. Linsley, in *Proceedings of the 18th International Cosmic Ray Conference*, Bangalore, India, 1983, edited by N. Durgaprasad *et al.* (TIFR, Bombay, 1983), Vol. 12, p. 135.

[9] H. T. Freudenreich *et al.*, Phys. Rev. D **41**, 2732 (1990); J. A. Goodman *et al.*, *ibid.* **26**, 1043 (1982).

[10] V. V. Akimov *et al.*, in *Proceedings of the International Cosmic Ray Conference*, Budapest [Acta Phys. Hung. Suppl. **29**, 517 (1969), Vol. 1]; V. V. Akimov *et al.*, *ibid.* **29**, 211 (1969); K. Asakimori *et al.*, in *Proceedings of the 22nd International Cosmic Ray Conference*, Dublin, Ireland 1991, (unpublished), Vol. 2, p. 97; J. A. Esposito *et al.*, Astrophys. J. **351**, 459 (1990); J. M. Grunsfeld, *ibid.* **327**, L31 (1988).

[11] MACRO Collaboration, M. Ambrosio *et al.*, in Proceedings of the 24th International Cosmic Ray Conference, Rome, Italy, 1995 (unpublished), Vol. 2, p. 689.

[12] M. Aglietta *et al.*, Phys. Lett. B **337**, 376 (1994).

[13] BAKSAN Collaboration, V. N. Bakatanov *et al.*, in Proceedings of the 24th International Cosmic Ray Conference [11], Vol. 2, p. 720.

[14] M. Aglietta *et al.*, in *Proceedings of the 21st International Cosmic Ray Conference*, Adelaide, Australia, 1990 (unpublished), Vol. 9, p. 352.

[15] G. J. Alner *et al.*, Phys. Lett. **167B**, 476 (1986).

[16] F. Abe *et al.*, Phys. Rev. Lett. **61**, 1819 (1988); F. Abe *et al.*, Phys. Rev. D **40**, 3791 (1989); G. J. Alner *et al.*, Phys. Rep. **154**, 247 (1987); R. E. Ansorge *et al.*, Phys. Lett. B **199**, 311 (1987).

[17] G. J. Alner *et al.*, Z. Phys. C **33**, 1 (1986).

[18] J. Whitmore, Phys. Rep., Phys. Lett. **C27**, 187 (1976).

[19] T. Yuda, in *Proceedings of the 22nd International Cosmic Ray Conference*, Dublin, Ireland, 1991, edited by M. Cawley *et al.* (Dublin Institute for Advanced Studies, Dublin, 1992), Vol. 5, p. 313.

[20] P. R. Vishwanath, Ph.D. thesis, University of Michigan, 1974; P. R. Vishwanath *et al.*, Phys. Lett. **53B**, 479 (1975).

[21] T. K. Gaisser and T. Stanev, Bartol Technical Report No. BA-82-1, 1982.

[22] P. S. Freir and C. J. Waddington, Astrophys. Space Sci. **38**, 419 (1975).